

Observation of a flat and extended surface state in a topological semimetal

Ryo Mori,^{1,2} Kefeng Wang,³ Takahiro Morimoto,^{4,5}

Jonathan D. Denlinger,⁶ Johnpierre Paglione,³ and Alessandra Lanzara^{2,7,*}

¹*Applied Science & Technology, University of California, Berkeley, California 94720, USA*

²*Materials Sciences Division, Lawrence Berkeley National Laboratory, Berkeley, California 94720, USA*

³*Maryland Quantum Materials Center, Department of Physics, University of Maryland, College Park, Maryland 20742, USA.*

⁴*Department of Applied Physics, The University of Tokyo, Hongo, Tokyo, 113-8656, Japan*

⁵*JST, PRESTO, Kawaguchi, Saitama, 332-0012, Japan*

⁶*Advanced Light Source, Lawrence Berkeley National Laboratory, Berkeley, California 94720, USA*

⁷*Department of Physics, University of California, Berkeley, California 94720, USA*

Abstract

A topological flatband, also known as drumhead states, is an ideal platform to drive new exotic topological quantum phases. Using angle-resolved photoemission spectroscopy experiments, we reveal the emergence of a highly localized possible drumhead surface state in a topological semimetal BaAl₄ and provide its full energy and momentum space topology. We find that the observed surface state is highly localized in momentum, inside a square-shaped bulk Dirac nodal loop, and in energy, leading to a flat band and a peak in the density of state. These results establish this class of materials as a possible experimental realization of drumhead surface states and provide an important reference for future studies of fundamental physics of topological quantum phase transition.

* To whom correspondence should be addressed. Email: ALanzara@lbl.gov

One notable class of the topological non-trivial states—nodal line semimetals—are the neighbor states to various topological quantum phases, such as three-dimensional Dirac semimetals, Weyl semimetals, topological insulators, spinful Weyl nodal line semimetals, and hence it is regarded as an ideal platform to study and control the quantum topological phase transition by breaking symmetries[1]. In a topological nodal line semimetal, the linearly degenerate bands cross each other on a mirror plane giving rise to a nodal line in the momentum space (see cartoon in Fig. 1(a)). The crossing bands on the mirror plane cannot hybridize since they have opposite mirror eigenvalues, resulting in a stable nodal loop/line on the mirror plane. The projection of these bulk nodal lines onto the surface fills the inside of the nodal lines and generates the so-called drumhead surface state[2–8], given its resemblance to the head of an open drum. The peculiar momentum space structure of these states, flat in both energy and momentum, is critical for the realization of novel phenomena[9–24], such as topological superconductivity[10, 12–14, 25] and magnetism[11]. In the case of superconductivity, for example, the momentum extension of the drumhead state (area) is proportional to the pairing strength, and hence T_c [10, 25]. Therefore, topological semimetals exhibiting drumhead surface states present a significant expansion of topological materials beyond topological insulators and nodal-point Dirac/Weyl semimetals.

Recently, BaAl_4 has been reported to have topological semimetallic features with 3D Dirac dispersions and possible nodal lines protected by crystal symmetry[26]. While this can explain several of the observed transport properties, it cannot fully account for the extremely large magnetoresistance, including quantum oscillations[26]. In this paper, we use angle-resolved photoemission spectroscopy (ARPES) to study in detail the electronic structure of BaAl_4 , focusing on the surface localized bands. BaAl_4 has the body-centered tetragonal structure in the space group of $I4/mmm$ (No. 139) as shown in Fig. 1(b), also known as a prototype parent crystal of a large family of compounds[26–30]. The bulk and (001) surface projected BZs with high-symmetry points labelled are shown in Fig. 1(c). The crystal has three non-equivalent mirror-reflection planes m_{001} (green and blue planes), m_{110} (orange plane), and m_{100} (red plane) (see Fig. 1(c)). The m_{110} plane and m_{100} plane have equivalent mirror planes along the orthogonal directions. Therefore, a number of Dirac nodal lines can exist on these planes when spin-orbit coupling (SOC) is negligible, leading to the presence of drumhead surface states.

Fig. 2 shows the bulk electronic structure of BaAl_4 . Panel (a) shows the theoretical bulk nodal lines without SOC. The energy and momentum dispersions along the high symmetry directions reveal the presence of several nodal points within the valence bands for each mirror plane (see dots in panel (b)). These nodal points, developing between the highest valence band and the second-highest valence band (Valence Gap (VG)), give rise to a variety of nodal lines in each mirror plane (see colored lines in panel (a)). The colors used in panels (a) and (b) for the nodal points/lines correspond to the same color scale used to represent the respective mirror plane (Fig. 1(c)). A detailed analysis of the irreducible representations for each crossing is shown in Supplementary Fig. 1 in the Supplementary Information (SI). Panels (c) and (d) show the calculated and experimental momentum and energy dispersions along the Σ_1-Z direction in the $k_z = 2\pi/c$ plane. Following the maximum intensity, a Dirac like linear-shaped dispersion can be observed, in agreement with the theoretical calculation in panel (c). The dispersion can be better extracted by following the peak positions in the momentum distribution curves (MDCs) shown in panel (e) where two peaks disperse

linearly throughout the entire energy range and cross at ~ -0.4 eV, namely the Dirac point. The non-gap linear feature is further confirmed in Supplementary Fig. 5 in the SI where the only one side of Dirac dispersion is observed due to the matrix element effect[31, 32]. Panels (f)-(h) show the same as panels (c)-(e), respectively, but the momentum direction is the Y_1-Z direction in the $k_z = 2\pi/c$ plane. Similar to the Σ_1-Z direction, the Dirac like linear dispersion can also be observed in the Y_1-Z direction and is confirmed by the MDCs spectra, where the two peaks disperse linearly and cross at the ED. Those Dirac nodes belong to one of the nodal loops in the $k_z = 2\pi/c$ plane (see the black arrows in panel (a)). The lack of a gap in the spectra can be due to the absence of hybridization between the two spins and/or weak SOC as in this case, where the bands near E_F in the VG region are mainly composed of Al s and p orbitals (see details in Supplementary Fig. 2 of the SI). Once SOC is introduced, the two spins are coupled and allowed to hybridize, resulting in a gap opening at each of the Dirac points/lines. This is true for each high symmetry directions, unless the $\Gamma-Z$ direction where the two bands belong to different representation of the symmetry group, and therefore, their intersection is protected by the crystalline symmetry, C_{4v} . The details of the crystal symmetric information and topological nature with SOC are found in Ref[26]. In the presence of weak SOC, the gap size becomes negligible, and this may be the case for the VG.

We now turn our attention to the surface localized electronic states. Thanks to the matrix element effect, the bulk and surface electronic structures can be characterized selectively (see the detail in Supplementary Fig. 4 in the SI). Fig. 3 shows the surface electronic structure within the surface BZ projected onto (001) plane. In addition to the bulk states identified in panel (b) (labelled as B1-B2), three new sets of features are observed in panel (a): sharp linearly dispersive states (labelled as S1-S2), a hole-like dispersion state (labelled as S3), and a weakly dispersive state (labelled as DS state). Similar features are observed in the surface states calculations shown in panel (b), pointing to their surface origin (see also Method section and Supplementary Fig. 3 in the SI for more details about the calculation). These multiple surface states, originating from the Dirac nodal lines, indicate their topologically protected nature. Note that the surface states calculation is sensitive to details of the simulations as reported[33], and surface effects, such as potential band bending and structural relaxation effects, are not included in the calculation. These effects might lead to apparent discrepancy between the experimental data (panel (a)) and theory (panel (b)). Other potential discrepancy could arise from matrix element effects[31, 32]. These effects can however be minimized by changing photon energy (see Supplementary Fig. 6 in the SI), revealing different features. The surface origin of these states is further supported by their photon energy dependence (i.e., k_z dependence) as shown in panels (c-f). Throughout the whole range, negligible dispersions are observed for each of these states, confirming their surface state origin. Indeed, S1 and S2 states form straight vertical lines as indicated by yellow arrows in panel (c) and blue dashed line in panel (e), indicative of lack of k_z dispersion. On the other hand, the DS state defines a sheet in the (k_y, k_z) plane (see dashed yellow rectangle in panel (d)), indicative of a localized state in k_z . This can be directly seen in panel (f), where the energy vs k_z dispersion along the $Z-\Gamma$ direction shows a localized two-dimensional state.

Among all the surface states, of particular interest is the DS state, which is the one appearing at $E = -0.49$ eV. Indeed, this state emerges out and connects the two Dirac bulk nodal lines, as expected in the case of a drumhead surface state (see also Fig. 3(a)). Fig. 4 presents its full momentum and energy characterization. The energy vs momentum

dispersion (panel (b)), extracted from the peak position of the energy distribution curves (EDC) (panel (a)), appears weakly dispersing along both the $\bar{\Gamma} - \bar{X}$ and $\bar{\Gamma} - \bar{M}$ direction, with an overall bandwidth less than 38 meV and 23 meV respectively in the momentum range ($k_1 - k_2$). This gives rise to an almost flat surface state with an effective mass of $m^* \simeq 4.0m_e$ and $6.1m_e$ and a peak in the density of state at the energy of the DS state (see the bold line in panel (a)). In panel (c), we show the momentum extension of the DS state. The constant energy map (k_y vs k_x) at DS state shows that the DS state is localized in momentum along a well-defined filled square-shaped region, centered at the BZ center. The topology of the DS state is consistent with the confirmed bulk nodal loop (see Fig. 2(a)) and is confined within an area of $\sim 0.16 \text{ \AA}^{-2}$, which corresponds to $\sim 8.5 \%$ of the BZ. Additionally, the momentum location of the surface states S2-S3 is also visible in this energy window. In contrast, the main contribution of the S1 state appears near E_F and is localized along a square-shaped region (see Supplementary Fig. S6 in the SI). The topology of these states is qualitatively consistent with the theoretical constant energy map shown in panel (d). All the data reported so far supports the existence of a strongly localized drumhead surface state in BaAl_4 and reveals its extended location in momentum space.

The localized nature of this state makes it unique with respect to previous studies[6, 34–36], where highly dispersive DS states have been reported. Indeed the flatness of our DS state drives a large density of states, as shown in Fig. 3–4, enhancing interaction effects significantly. The large area of the DS state is also promising in view of the enhancing the electrons’ interaction[10, 25], although the first step would be to engineer the DS state close to the Fermi level. Finally, it is noteworthy to point out that the observed bulk nodal line might be also responsible for the reported transport anomaly, including the quantum oscillation and extremely large magnetoresistance[26]. A complete quantification of the gap size in BaAl_4 , and hence the topological classification of BaAl_4 , requires more detailed calculations and further measurements. Even a small amount of lattice strain can tune the gap size[37–41], resulting in a new type of Dirac semimetal, where both Dirac point and Dirac nodal lines may coexist.

In summary, by combining surface-sensitive ARPES experiments with the theoretical calculations, we have provided direct evidence for the existence of a flat extended surface state in a topological semimetal, BaAl_4 . We present that the flat surface state fills inside of the bulk square-shaped nodal line by showing the full momentum space topology of such state. All the data reported here support that the observed flat band is directly associated with the observed Dirac nodal line, and therefore, the topological drumhead surface states. These results enable the exploration of such states for the realization of a number of novel correlated phases of matter[9–14, 16, 20–22, 25, 42].

Methods

Single crystals of BaAl_4 were synthesized by a high-temperature self-flux method and characterized by X-ray diffraction at room temperature with Cu K_α ($\lambda = 0.15418$ nm) radiation in a powder diffractometer[26].

Electronic structure calculations were performed within the framework of the density functional theory (DFT) with the PAW pseudopotentials, as implemented in the Quantum Espresso package[43]. The generalized gradient approximation (GGA) with the Perdew-Burke-Ernzerhof parameterization (PBE) was used[44]. A plane wave energy cut-off 40 Ry and $24 \times 24 \times 24$ k -mesh to sample the BZ were used for the bulk calculations. Total energies were converged to smaller than 10^{-10} . The experimental crystal data ($a = b = 4.566$ Å, $c = 11.278$ Å) were used[45]. The calculation of surface electronic structures was carried out with momentum resolved local density of states of a semi-infinite surface by employing a tight-binding (TB) model obtained by using the Wannier90[46] and WannierTools suite of code[47]. The quality of the Wannier function based TB model was checked by comparing it with the DFT calculation (see Supplementary Fig. S3 in the SI). The comparison of our experimental spectra with the theory-calculated surface states shows a good agreement with a 25 % expansion in the energy dimension of the calculation result. VESTA package was used for visualization of the crystal structure[48].

ARPES measurements on single crystalline samples of BaAl_4 were performed at the Beamline 4.0.3. end station of the Advanced Light Source in Berkley California. Samples were cleaved in situ to yield clean (001) surfaces and measured at 20 K in an ultra-high vacuum better than 3×10^{-11} Torr using the photon energy of 80-128 eV with Scienta R8000 analyzer. The energy resolution was 20-30 meV and the angular resolution was better than 0.2° for all measurements. According to this photon energy dependence measurements, the inner potential of BaAl_4 is estimated to 10.5 eV.

Acknowledgments

This work was primarily funded by the U.S. Department of Energy, Office of Science, Office of Basic Energy Sciences, Materials Sciences and Engineering Division under Contract No. DE-AC02-05-CH11231 (Quantum materials KC2202) and used resources of the Advanced Light Source, a DOE Office of Science User Facility under contract no. DE-AC02-05CH11231. Research at the University of Maryland was supported by the Gordon and Betty Moore Foundation's EPiQS Initiative through Grant No. GBMF9071, and the Maryland Quantum Materials Center. TM was supported by JST PRESTO (JPMJPR19L9), and JST CREST (JPMJCR19T3).

Author contributions

A.L., J.P., and R.M. initiated and directed this research project. R.M. carried out ARPES measurements with the assistance of J.D.D. R.M. calculated the band structure and analyzed the ARPES data. A.L. and R.M. wrote the text, with feedback from all authors. The samples were grown and characterized by K.W. T.M. provided theoretical insight.

Competing Interests

The authors declare that they have no competing financial interests.

Correspondence

Correspondence and requests for materials should be addressed to A.L. (email: alan-zara@lbl.gov).

Data availability

The data that support the finding of this study are available from the corresponding author upon request.

-
- [1] Yang, S.-Y. *et al.* Symmetry demanded topological nodal-line materials. *Advances in Physics: X* **3**, 1414631 (2018). URL <https://doi.org/10.1080/23746149.2017.1414631>.
 - [2] Chiu, C.-K., Teo, J. C. Y., Schnyder, A. P. & Ryu, S. Classification of topological quantum matter with symmetries. *Rev. Mod. Phys.* **88**, 035005 (2016). URL <https://link.aps.org/doi/10.1103/RevModPhys.88.035005>.
 - [3] Burkov, A. A., Hook, M. D. & Balents, L. Topological nodal semimetals. *Phys. Rev. B* **84**, 235126 (2011). URL <https://link.aps.org/doi/10.1103/PhysRevB.84.235126>.
 - [4] Zhao, Y. X. & Wang, Z. D. Topological classification and stability of Fermi surfaces. *Phys. Rev. Lett.* **110**, 240404 (2013). URL <https://link.aps.org/doi/10.1103/PhysRevLett.110.240404>.
 - [5] Ryu, S. & Hatsugai, Y. Topological origin of zero-energy edge states in particle-hole symmetric systems. *Phys. Rev. Lett.* **89**, 077002 (2002). URL <https://link.aps.org/doi/10.1103/PhysRevLett.89.077002>.
 - [6] Bian, G. *et al.* Topological nodal-line fermions in spin-orbit metal PbTaSe₂. *Nature Communications* **7**, 10556 (2016). URL <http://dx.doi.org/10.1038/ncomms10556>.
 - [7] Kim, Y., Wieder, B. J., Kane, C. L. & Rappe, A. M. Dirac line nodes in inversion-symmetric crystals. *Phys. Rev. Lett.* **115**, 036806 (2015). URL <https://link.aps.org/doi/10.1103/PhysRevLett.115.036806>.
 - [8] Ma, J. F. B. Y. Z.-M. L. C.-C. Y. Y., Da-Shuai; Zhou. Mirror protected multiple nodal line semimetals and material realization. *arXiv:1804.06960* (2018). URL <https://arxiv.org/abs/1809.10726>.
 - [9] Tang, E. & Fu, L. Strain-induced partially flat band, helical snake states and interface superconductivity in topological crystalline insulators. *Nature Physics* **10**, 964 (2014). URL <http://dx.doi.org/10.1038/nphys3109>.
 - [10] Kopnin, N. B., Heikkilä, T. T. & Volovik, G. E. High-temperature surface superconductivity in topological flat-band systems. *Phys. Rev. B* **83**, 220503 (2011). URL <https://link.aps.org/doi/10.1103/PhysRevB.83.220503>.
 - [11] Magda, G. Z. *et al.* Room-temperature magnetic order on zigzag edges of narrow graphene nanoribbons. *Nature* **514**, 608 (2014). URL <http://dx.doi.org/10.1038/nature13831>.
 - [12] Shapourian, H., Wang, Y. & Ryu, S. Topological crystalline superconductivity and second-order topological superconductivity in nodal-loop materials. *Phys. Rev. B* **97**, 094508 (2018). URL <https://link.aps.org/doi/10.1103/PhysRevB.97.094508>.

- [13] Sur, S. & Nandkishore, R. Instabilities of weyl loop semimetals. *New Journal of Physics* **18**, 115006 (2016). URL <http://dx.doi.org/10.1088/1367-2630/18/11/115006>.
- [14] Wang, Y. & Nandkishore, R. M. Topological surface superconductivity in doped weyl loop materials. *Phys. Rev. B* **95**, 060506 (2017). URL <https://link.aps.org/doi/10.1103/PhysRevB.95.060506>.
- [15] Imada, M. & Kohno, M. Superconductivity from flat dispersion designed in doped mott insulators. *Phys. Rev. Lett.* **84**, 143–146 (2000). URL <https://link.aps.org/doi/10.1103/PhysRevLett.84.143>.
- [16] Peotta, S. & Törmä, P. Superfluidity in topologically nontrivial flat bands. *Nature Communications* **6**, 8944 (2015). URL <http://dx.doi.org/10.1038/ncomms9944>.
- [17] Huber, S. D. & Altman, E. Bose condensation in flat bands. *Phys. Rev. B* **82**, 184502 (2010). URL <https://link.aps.org/doi/10.1103/PhysRevB.82.184502>.
- [18] Wu, C., Bergman, D., Balents, L. & Das Sarma, S. Flat bands and wigner crystallization in the honeycomb optical lattice. *Phys. Rev. Lett.* **99**, 070401 (2007). URL <https://link.aps.org/doi/10.1103/PhysRevLett.99.070401>.
- [19] Tasaki, H. Ferromagnetism in the hubbard models with degenerate single-electron ground states. *Phys. Rev. Lett.* **69**, 1608–1611 (1992). URL <https://link.aps.org/doi/10.1103/PhysRevLett.69.1608>.
- [20] Wang, M. X. *et al.* Nodeless superconducting gaps in noncentrosymmetric superconductor PbTaSe₂ with topological bulk nodal lines. *Phys. Rev. B* **93**, 020503 (2016). URL <https://link.aps.org/doi/10.1103/PhysRevB.93.020503>.
- [21] Sun, K., Gu, Z., Katsura, H. & Das Sarma, S. Nearly flatbands with nontrivial topology. *Phys. Rev. Lett.* **106**, 236803 (2011). URL <https://link.aps.org/doi/10.1103/PhysRevLett.106.236803>.
- [22] Neupert, T., Santos, L., Chamon, C. & Mudry, C. Fractional quantum hall states at zero magnetic field. *Phys. Rev. Lett.* **106**, 236804 (2011). URL <https://doi.org/10.1103/PhysRevLett.106.236804>.
- [23] Pezzini, S. *et al.* Unconventional mass enhancement around the dirac nodal loop in ZrSiS. *Nature Physics* **14**, 178 (2017). URL <http://dx.doi.org/10.1038/nphys4306>.
- [24] Matusiak, M., Cooper, J. R. & Kaczorowski, D. Thermoelectric quantum oscillations in ZrSiS. *Nature Communications* **8**, 15219 (2017). URL <http://dx.doi.org/10.1038/ncomms15219>.
- [25] Volovik, G. E. From standard model of particle physics to room-temperature superconductivity. *Physica Scripta* **2015**, 014014 (2015). URL <http://stacks.iop.org/1402-4896/2015/i=T164/a=014014>.
- [26] Wang, K. *et al.* Crystalline symmetry-protected non-trivial topology in prototype compound baal4. *npj Quantum Materials* **6**, 28 (2021). URL <https://doi.org/10.1038/s41535-021-00325-6>.
- [27] Paglione, J. & Greene, R. L. High-temperature superconductivity in iron-based materials. *Nature Physics* **6**, 645–658 (2010). URL <https://doi.org/10.1038/nphys1759>.
- [28] Steglich, F. *et al.* Superconductivity in the presence of strong pauli paramagnetism: CeCu₂Si₂. *Phys. Rev. Lett.* **43**, 1892–1896 (1979). URL <https://link.aps.org/doi/10.1103/PhysRevLett.43.1892>.
- [29] Stewart, G. R. Heavy-fermion systems. *Rev. Mod. Phys.* **56**, 755–787 (1984). URL <https://link.aps.org/doi/10.1103/RevModPhys.56.755>.
- [30] Kneidinger, F. *et al.* Superconductivity in noncentrosymmetric Baal₄ derived structures. *Phys. Rev. B* **90**, 024504 (2014). URL <https://link.aps.org/doi/10.1103/PhysRevB.90>.

- 024504.
- [31] Chen, Y. Studies on the electronic structures of three-dimensional topological insulators by angle resolved photoemission spectroscopy. *Frontiers of Physics* **7**, 175–192 (2012). URL <https://doi.org/10.1007/s11467-011-0197-9>.
 - [32] Damascelli, A., Hussain, Z. & Shen, Z.-X. Angle-resolved photoemission studies of the cuprate superconductors. *Rev. Mod. Phys.* **75**, 473–541 (2003). URL <https://link.aps.org/doi/10.1103/RevModPhys.75.473>.
 - [33] Cucchi, I. *et al.* Bulk and surface electronic structure of the dual-topology semimetal Pt_2HgSe_3 . *Phys. Rev. Lett.* **124**, 106402 (2020). URL <https://link.aps.org/doi/10.1103/PhysRevLett.124.106402>.
 - [34] Belopolski, I. *et al.* Discovery of topological weyl fermion lines and drumhead surface states in a room temperature magnet. *Science* **365**, 1278 (2019). URL <https://science.sciencemag.org/content/365/6459/1278>.
 - [35] Lou, R. *et al.* Experimental observation of bulk nodal lines and electronic surface states in zrB_2 . *npj Quantum Materials* **3**, 43 (2018). URL <https://doi.org/10.1038/s41535-018-0121-4>.
 - [36] Muechler, L. *et al.* Modular arithmetic with nodal lines: Drumhead surface states in zrSiTe . *Phys. Rev. X* **10**, 011026 (2020). URL <https://link.aps.org/doi/10.1103/PhysRevX.10.011026>.
 - [37] Tang, E., Mei, J.-W. & Wen, X.-G. High-temperature fractional quantum hall states. *Phys. Rev. Lett.* **106**, 236802 (2011). URL <https://link.aps.org/doi/10.1103/PhysRevLett.106.236802>.
 - [38] Winterfeld, L. *et al.* Strain-induced topological insulator phase transition in HgSe . *Phys. Rev. B* **87**, 075143 (2013). URL <https://link.aps.org/doi/10.1103/PhysRevB.87.075143>.
 - [39] Rodin, A. S., Carvalho, A. & Castro Neto, A. H. Strain-induced gap modification in black phosphorus. *Phys. Rev. Lett.* **112**, 176801 (2014). URL <https://link.aps.org/doi/10.1103/PhysRevLett.112.176801>.
 - [40] Teshome, T. & Datta, A. Phase coexistence and strain-induced topological insulator in two-dimensional BiAs. *J. Phys. Chem. C* **122**, 15047–15054 (2018). URL <https://doi.org/10.1021/acs.jpcc.8b05293>.
 - [41] Owerre, S. A. Strain-induced topological magnon phase transitions: applications to kagome-lattice ferromagnets. *Journal of Physics: Condensed Matter* **30**, 245803 (2018). URL <http://stacks.iop.org/0953-8984/30/i=24/a=245803>.
 - [42] BERGHOLTZ, E. M. I. L. J. & L. I. U., Z. H. A. O. Topological flat band models and fractional chern insulators. *Int. J. Mod. Phys. B* **27**, 1330017 (2013). URL <https://doi.org/10.1142/S021797921330017X>.
 - [43] Giannozzi, P. *et al.* QUANTUM ESPRESSO: a modular and open-source software project for quantum simulations of materials. *Journal of Physics: Condensed Matter* **21**, 395502 (2009). URL <http://stacks.iop.org/0953-8984/21/i=39/a=395502>.
 - [44] Perdew, J. P., Burke, K. & Ernzerhof, M. Generalized gradient approximation made simple. *Phys. Rev. Lett.* **77**, 3865–3868 (1996). URL <http://dx.doi.org/10.1103/PhysRevLett.77.3865>.
 - [45] Bruzzone, G. & Merlo, F. The strontium-aluminium and barium-aluminium systems. *Journal of the Less Common Metals* **39**, 1–6 (1975). URL <http://www.sciencedirect.com/science/article/pii/002250887590212X>.
 - [46] Mostofi, A. A. *et al.* An updated version of wannier90: A tool for obtaining maximally-localised wannier functions. *Computer Physics Communications* **185**, 2309–2310 (2014). URL

<https://doi.org/10.1016/j.cpc.2014.05.003>.

- [47] Wu, Q., Zhang, S., Song, H.-F., Troyer, M. & Soluyanov, A. A. WannierTools: An open-source software package for novel topological materials. *Computer Physics Communications* **224**, 405–416 (2018). URL <https://doi.org/10.1016/j.cpc.2017.09.033>.
- [48] Momma, K. & Izumi, F. VESTA 3 for three-dimensional visualization of crystal, volumetric and morphology data. *J. Appl. Cryst.* **44**, 1272–1276 (2011). URL <https://doi.org/10.1107/S0021889811038970>.

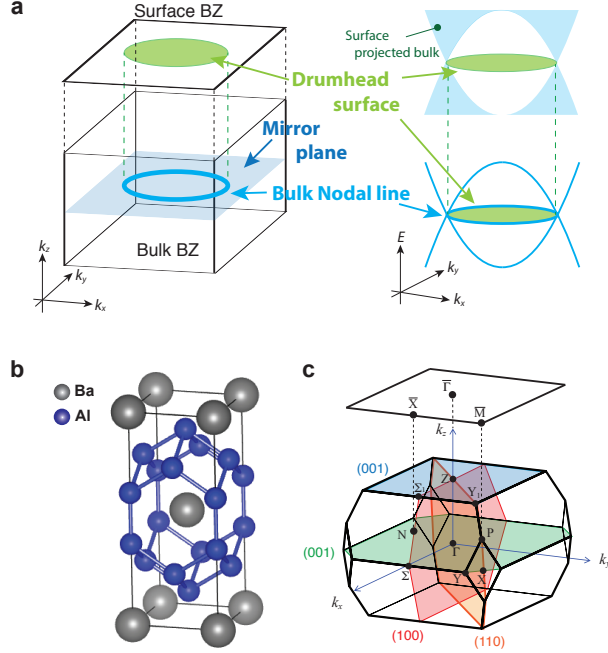


FIG. 1. **Topological drumhead surface states and crystal structure of the topological semimetal BaAl_4 .** **a**, Schematics of a bulk Dirac nodal line and a drumhead surface state in a topological semimetal in the momentum space (left panels) and in the energy and momentum space (right panels). A gap closing line (light blue solid line) appears in the momentum space, protected by a crystal mirror plane (dark blue plane). Surface states appear inside of the gap closing line, forming the drumhead surface states (light green plane). **b**, The crystal structure of BaAl_4 . The gray and the blue spheres represent the Ba and the Al atoms, respectively. **c**, The bulk Brillouin zone (BZ) and the (001) surface BZ, marked with high-symmetry points. In the bulk structure, the three non-equivalent mirror-reflection planes m_{001} (green plane ($k_z = 0$)) and blue plane ($k_z = 2\pi/c$)), m_{110} (orange plane), and m_{100} (red plane) are illustrated.

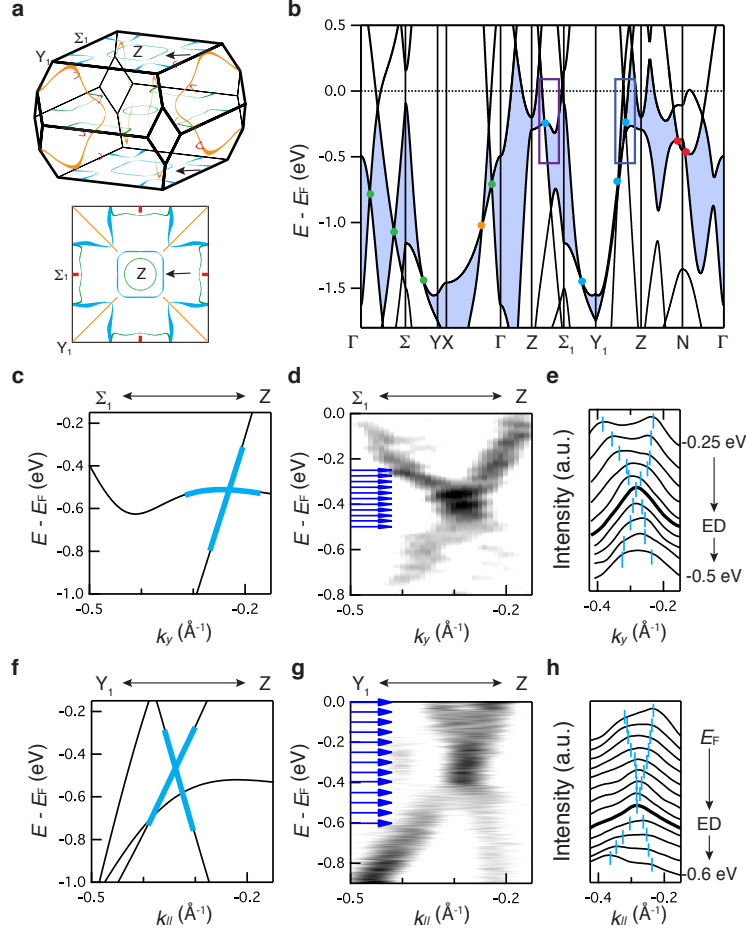


FIG. 2. **Bulk electronic structure of topological semimetal BaAl₄.** **a,b**, The bulk Dirac nodal lines in bulk BZ (top in **a**) and on the (001) surface projected BZ (bottom in **a**) and the calculated bulk electronic structure near E_F without spin-orbit coupling (SOC) (**b**). The black arrows in **a** mark the experimentally identified nodal line in this work. The blue shaded region in **b** is the energy gap between the highest valence band and the second-highest valence band where the nodal lines shown in this work exist. The blue and purple squares highlight the experimentally observed nodal line in this work. Each color of nodal lines/points in **a,b** represents the corresponding mirror plane shown in Fig. 1c. **c,f**, Zoom in of the calculated electronic structure along Σ_1-Z (**c**) and Y_1-Z (**d**) direction in $k_z = 2\pi/c$ plane protected by m_{100} (see the purple and blue squares in **b**). The solid light blue lines in the calculation are guides to the eye for the Dirac band-crossing. **d,g**, The experimental electronic structure (second-derivative in momentum direction) along Σ_1-Z (**d**) and Y_1-Z (**g**) direction, respectively. **e,h**, The momentum distribution curves (MDCs) along the cuts along Σ_1-Z (see blue arrows from -0.25 eV to -0.5 eV in **d**) (**e**) and the cuts along Y_1-Z (see blue arrows from E_F to -0.6 eV in **g**) (**f**), respectively, showing the Dirac dispersion of the nodal line. The light blue marks indicate the peak positions. The bold black lines highlight MDC near the energy of Dirac point (ED).

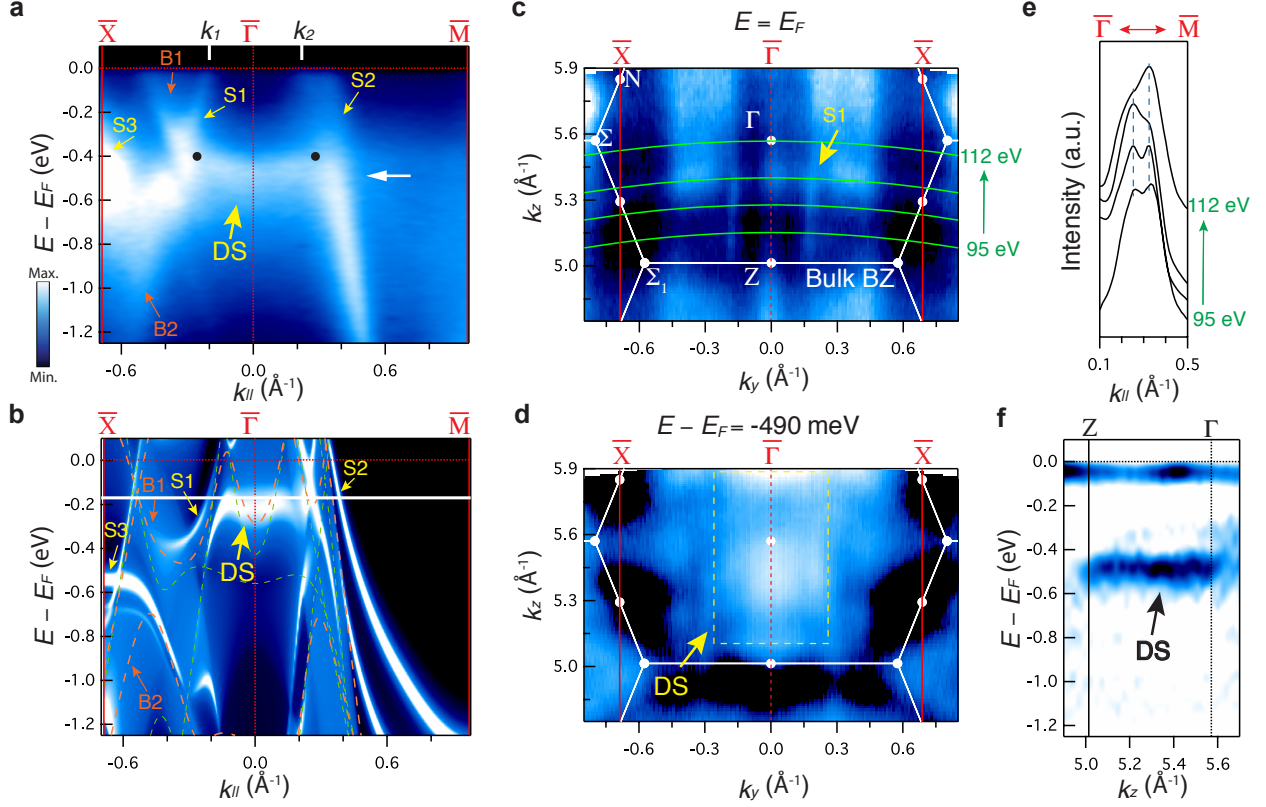


FIG. 3. **Surface states of BaAl₄.** **a**, ARPES spectra of energy versus momentum cuts along the high-symmetry directions $\bar{X} - \bar{\Gamma} - \bar{M}$ with photon energies 95 eV. The orange and yellow arrows mark the observed bulk (B1-B2) and surface (S1-S3 and DS) states, respectively. The black dots represent the bulk Dirac nodes obtained from the bulk experimental results (Fig. 2). **b**, Calculated surface band structure along high-symmetry direction $\bar{X} - \bar{\Gamma} - \bar{M}$ of BaAl₄ (001) surface for a semi-infinite slab. The orange dashed lines represent calculated bulk band structures without SOC for k_z corresponding to the photon energy of 95 eV. The light-green dashed lines are calculated bulk for $k_z = 2\pi/c$. **c**, ARPES spectral intensity map in the $k_z - k_y$ plane at the $E = E_F$. The k_z range covers half of the bulk BZ and corresponds to a photon energy range of 95–112 eV. The green solid lines represent the location of the cuts studied in this work. From bottom to top, each line corresponds to 95, 100, 105, and 112 eV of photon energy, respectively. **d**, ARPES spectral intensity map in the $k_z - k_y$ plane at the binding energy $E = -490$ meV shown by the white arrow in panel **a**. The yellow dashed rectangle represents the DS state. **e**, MDCs of spectra along $\bar{\Gamma} - \bar{M}$ direction at $E = E_F$ for different photon energies represented in **c**. The blue dashed lines represent the estimated peak positions. **f**, Second derivative of energy versus k_z intensity plot.

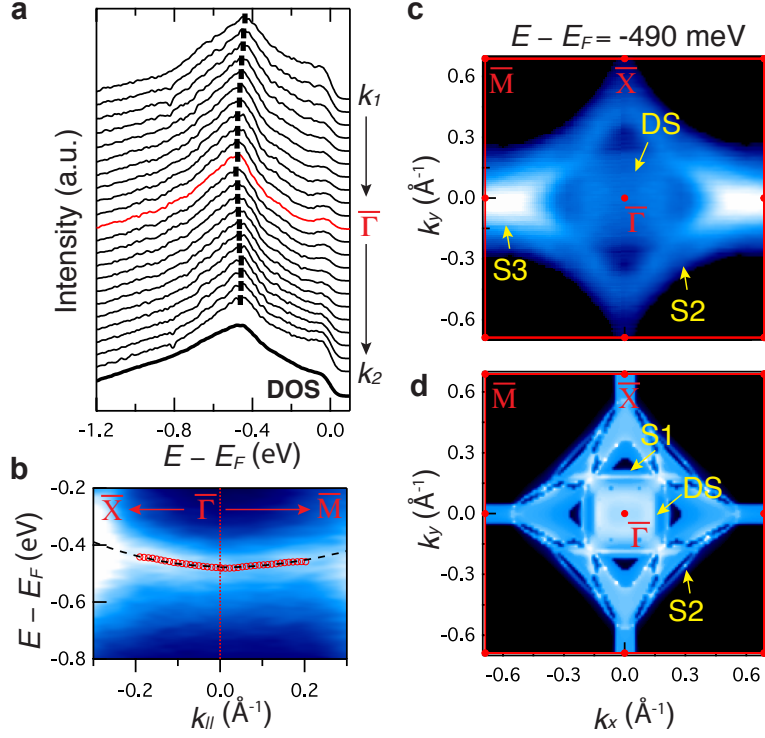
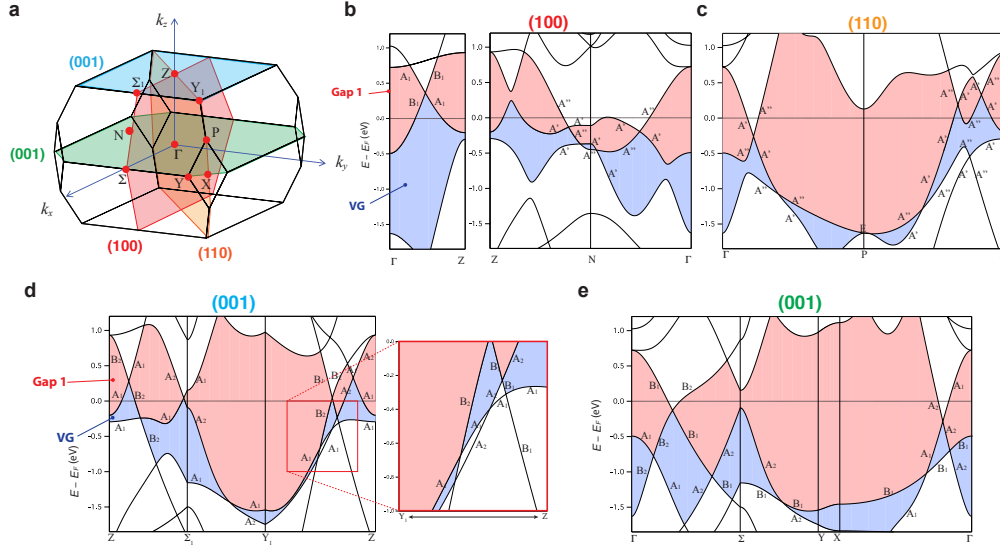
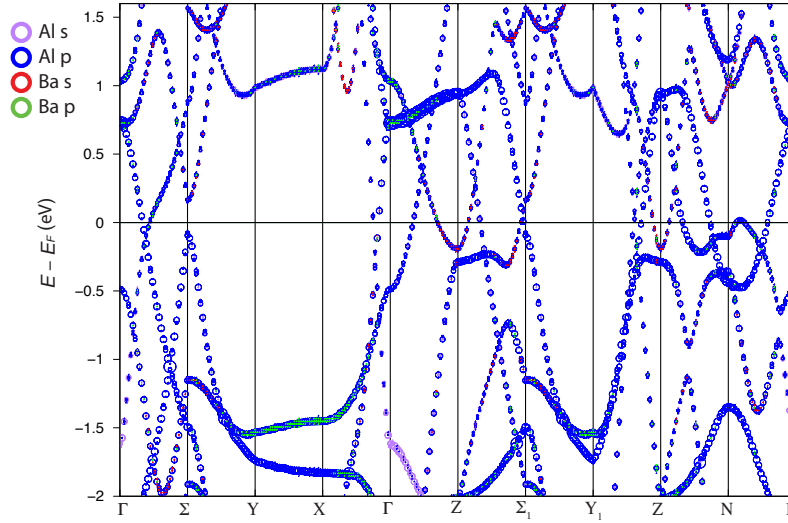


FIG. 4. **Full mapping of the topological drumhead surface state.** **a**, EDCs from k_1 to k_2 at the position indicated by the marks in Fig. 3a. The bold line at the bottom is the integrated density of state (DOS). **b**, Extracted dispersions of the drumhead state along $\bar{X} - \bar{\Gamma} - \bar{M}$ (the red dots) and the fitting (the black dashed-line). **c**, Constant energy maps at $E = -0.49$ eV. The surface states (S2-S3) and the drumhead surface (DS) state are marked by the yellow arrows. **d**, Calculated energy contour at the energy marked by white solid line in Fig. 3c.

Supplementary Note 1: Irreducible representations of crossing points



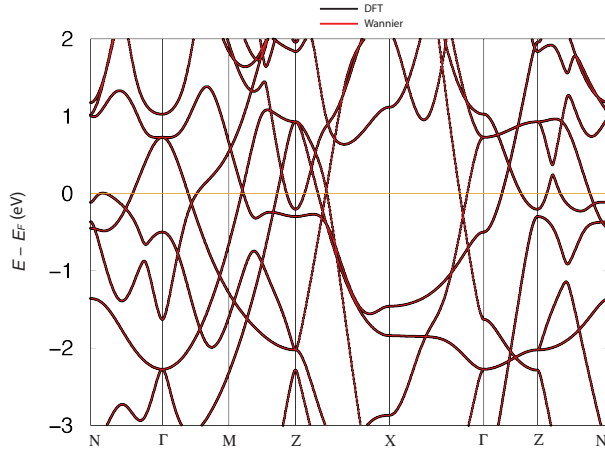
Supplementary Note 2: Orbital contribution near E_F



Supplementary Fig. 2. Calculated electronic structures with orbital weight. DFT calculated band structure with orbital weight. The size of the dots is proportional to the relative amplitude of the weight of orbital projection onto Al-*s* (purple), Al-*p* (blue), Ba-*s* (red), and Ba-*p* (green) orbitals. Ba *s* and *p* orbitals are represented by red and green. The Fermi level is set to zero.

To see the orbital contribution for the band structures near E_F , the orbital projected band dispersions are calculated as shown in Supplementary Fig. 2. The size of circles represents the relative weight of orbital projection onto Al-*p*, Al-*s*, Ba-*s*, and Ba-*p* orbitals. The bands near E_F are composed mainly of Al-*p* and Al-*s* orbital, resulting in small SOC effects. Once SOC is included in the calculation, hybridization leads to gap opening. The size of the gap is directly related to the strength of SOC.

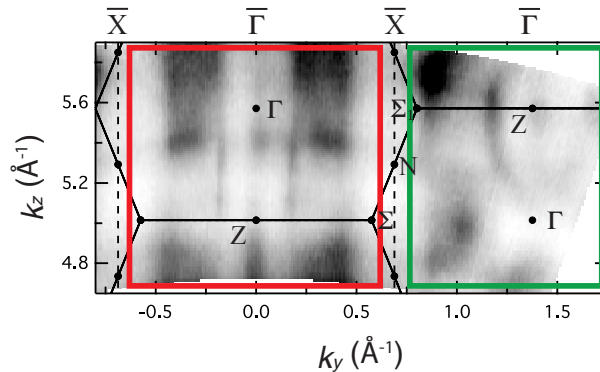
Supplementary Note 3: Wannier function for tight-binding



Supplementary Fig. 3. Comparison Wannier function based tight-binding model with DFT. Band structure from Wannier function based tight-binding model (red) and DFT (black). Wannier effective tight-binding model reproduces all the features calculated with DFT.

To help understand the observed electronic structures in the main text, we create Wannier function based tight-binding model. Supplementary Fig. 3 shows the band dispersions based on DFT (black lines) and Wannier functions (red lines). This tight-binding model can well reproduce the energy bands near E_F , which are crucial to the band topology. This Wannier function-based model is used in the surface electronic structure calculation shown in the main text.

Supplementary Note 4: Bulk and surface electronic structures

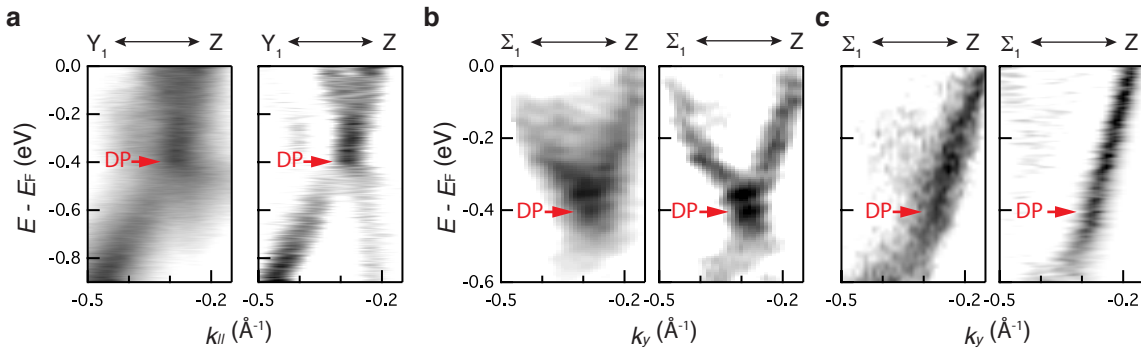


Supplementary Fig. 4. ARPES spectral intensity map in the $k_z - k_y$ plane at the $E = E_F$ for wide momentum range. The black solid (dashed) lines represent the bulk (surface) BZ. The red and green square mark the surface and bulk sensitive region in BZ, respectively.

Thanks to the matrix element effect, the bulk and surface electronic structures can be

characterized selectively. In Supplementary Fig. 4, we show the out-of-plane Fermi surface mapping taken with the different photon energies. In the red square region in the panel, negligible dispersions are observed throughout the whole range, confirming their surface state origin. On the contrary, the dispersive electronic structures are observed in the different BZ (see the green square region), suggesting their bulk state origin. The observed bulk states here are consistent well with the calculated Fermi surface (see Ref[26] for more details about the bulk structure).

Supplementary Note 5: Bulk Dirac nodes



Supplementary Fig. 5. ARPES spectra of the bulk electronic structure. **a** ARPES spectra (left) and its second derivative in momentum (right) along Y_1 -Z direction. **b** ARPES spectra (left) and its second derivative in momentum (right) along Σ_1 -Z direction. **c** ARPES spectra (left) and its second derivative in momentum (right) along Σ_1 -Z direction, taken in the different BZ from **b**. The red arrows show the Dirac point (DP).

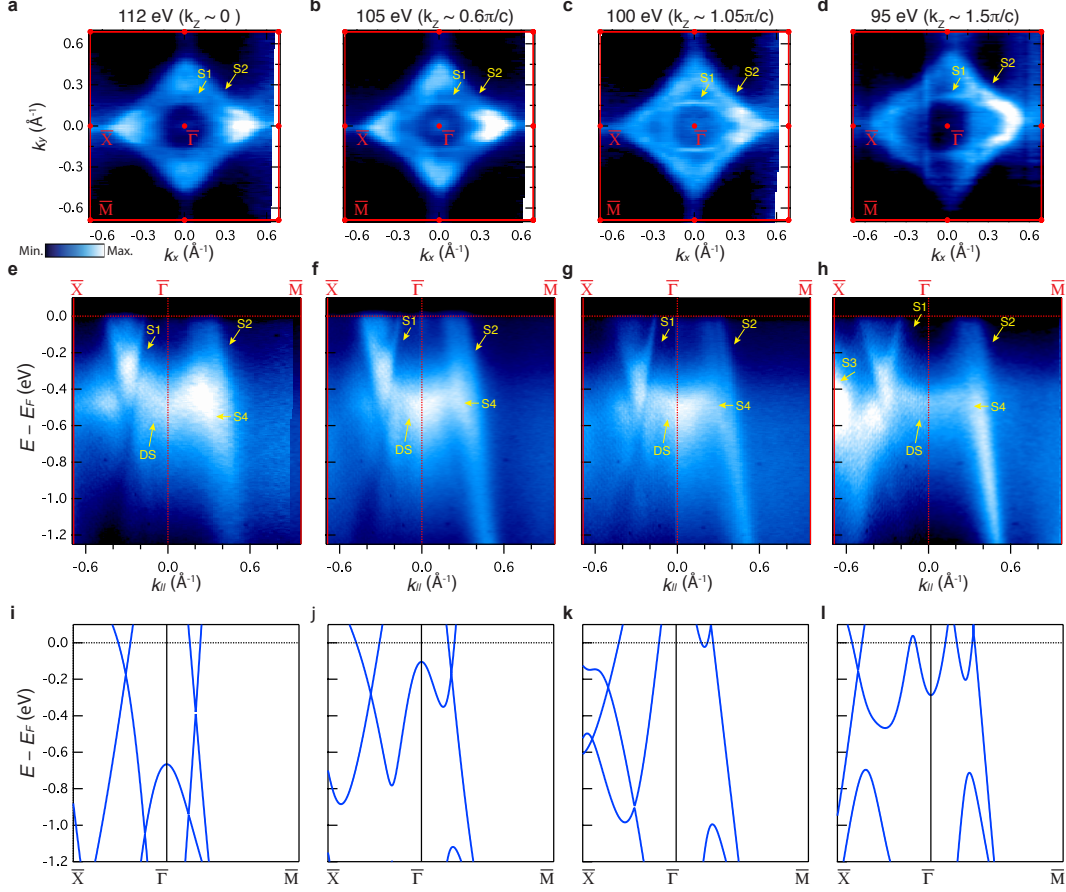
As shown in Fig. 2 in the main text, the bulk Dirac nodes along two high-symmetric lines in $k_z = 2\pi/c$ plane are observed. Supplementary Fig. 5(a)-(b) show the raw normalized spectra and their second derivative along Y_1 -Z direction. and Σ_1 -Z, respectively. Panel (c) shows the experimental result along Σ_1 -Z direction (the same direction as panel (b)), but taken in the different BZ. In this BZ, the only one side of Dirac dispersion is observed due to the matrix element effect, further confirming the non-gap linear dispersion.

Supplementary Note 6: Photon energy dependence of bulk and surface states

Photon energy dependence is a powerful way to extract the k_z dependence of electronic structures. The k_z dependence can be obtained by changing photon energy using the free-electron final state approximation:

$$k_z = \frac{1}{\hbar} \sqrt{2m_e(E_i + h\nu - \Phi) \cos \theta + V_0} \quad (1)$$

where m_e is the free electron mass, E_i is the energy of the initial state, $h\nu$ is the photon energy, Φ is the work function, θ is the emission angle of photoelectrons, and V_0 is the inner potential. Electronic structures taken with the different photon energies resolve the surface nature of the observed spectra; surface states are two-dimensional states and hence showing no k_z dependence, while bulk states show k_z dispersive three-dimensional feature.



Supplementary Fig. 6. ARPES spectra with different photon energies and corresponding calculated bulk bands. a–d Fermi surface mappings with different photon energies 112 (a), 105 (b), 100 (c), and 95 (d) eV. e–h ARPES spectra of energy versus momentum cuts along the high-symmetry directions with photon energies 112 (a), 105 (b), 100 (c), and 95 (d) eV. i–l Calculated bulk band structures without SOC. Each structure is calculated for k_z corresponding to each photon energy; $k_z \sim 0$ ($h\nu = 112$ eV in (i)), $k_z \sim -0.6\pi/c$ ($h\nu = 105$ eV in (j)), $k_z \sim -1.05\pi/c$ ($h\nu = 100$ eV in (k)), and $k_z \sim -1.5\pi/c$ ($h\nu = 95$ eV in (l)).

Supplementary Fig. 6 shows the experimental spectra (panels (a–h)) and the calculated bulk structures for several different photon energies, corresponding to different k_z values in panels (i–l); $k_z \sim 0$ ($h\nu = 112$ eV in (i)), $k_z \sim -0.6\pi/c$ ($h\nu = 105$ eV in (j)), $k_z \sim -1.05\pi/c$ ($h\nu = 100$ eV in (k)), and $k_z \sim -1.5\pi/c$ ($h\nu = 95$ eV in (l)). The Fermi surface mappings (panels (a)–(d)) confirm that the topology of the observed surface states (S1–S2) near E_F is consistent with the theoretical constant energy map shown in Fig. 4(d) in the main text. By comparing the experimental spectra (panels (e)–(h)) and the bulk calculations (panels (i)–(l)), the S1–S4 states and the DS state are clearly distinguished from the bulk electronic features, validating their surface origins. Note that the matrix element effects play a different role for different photon energy, leading to the different appearance of these states. Indeed, S4 appears in panels (e)–(g) and the intensity is suppressed in panel (h), and S3 appears in panel (h).